

Supporting Information

Towards the Circular Economy: Converting Aromatic Plastic Waste Back to Arenes over a Ru/Nb₂O₅ Catalyst

Yaxuan Jing, Yanqin Wang, Shinya Furukawa, Jie Xia, Chengyang Sun, Max J. Hülsey, Haifeng Wang, Yong Guo, Xiaohui Liu, and Ning Yan**

anie_202011063_sm_miscellaneous_information.pdf

Contents

| | |
|---|----|
| Experimental procedures | 3 |
| Catalyst preparation | 3 |
| Catalytic test and product analysis..... | 3 |
| Characterization | 4 |
| Computational details | 6 |
| Table S1. Elemental analysis results of various aromatic plastics..... | 7 |
| Table S2. The conversion of methyl p-toluate and methyl 4-ethylcyclohexanecarboxylate over Ru/Nb ₂ O ₅ | 9 |
| Table S3. The conversion of Coca-Cola bottle over Ru/Nb ₂ O ₅ | 10 |
| Table S4 The catalytic conversion of PET and PS over Nb ₂ O ₅ and without catalyst..... | 11 |
| Table S5. Elemental analysis results of various solids. | 12 |
| Table S6. Ru contents and dispersions in various catalysts. | 13 |
| Table S7. EXAFS fitting results of the Ru K-edge for Ru/TiO ₂ and Ru/ZSM-5..... | 14 |
| Table S8. The conversion of diphenylmethane over Ru/Nb ₂ O ₅ and Ru/HZSM-5..... | 15 |
| Table S9. The amount of Brønsted and Lewis acid sites on Nb ₂ O ₅ and HZSM-5..... | 16 |
| Scheme S1. Proposed reaction pathway for the conversion of PET..... | 17 |
| Figure S1. View of representative C-O and C-C linkages of biomass and aromatic plastics..... | 18 |
| Figure S2. IR results of various plastics | 19 |
| Figure S3. TEM images, XRD patterns N ₂ adsorption-desorption isotherms and the BJH pore size distribution curves and Ru/Nb ₂ O ₅ | 20 |
| Figure S4. The direct conversion of PET over various catalysts. | 21 |
| Figure S5. The conversion of methyl 4-methylcyclohexanecarboxylate over various catalysts.. .. | 22 |
| Figure S6. Influence of reaction conditions in the conversion of PET over Ru/Nb ₂ O ₅ | 23 |
| Figure S7. The observations for dispersity of PPO in water and octane..... | 25 |
| Figure S8. The conversion of mixed plastics with different concentration of substrate and different substrate/catalyst mass ratio. | 26 |
| Figure S9. Recyclability test of Ru/Nb ₂ O ₅ for the conversion of mixed plastics. | 27 |
| Figure S10. XRD patterns of various catalysts and their larger versions (35-50 ° and 55-75°). | 28 |
| Figure S11. EXAFS spectra of Ru/TiO ₂ and Ru/ZSM-5. | 29 |
| Figure S12. XANES simulation for Ru foil based on DFT calculation..... | 30 |
| Figure S13. Py-FTIR spectra collected after treatment at 100 °C under vacuum of Nb ₂ O ₅ | 31 |

| | |
|---|-----------|
| Figure S14 Toluene DRIFTS spectra of Ru/Nb ₂ O ₅ and Nb ₂ O ₅ | 32 |
| Figure S15 The optimization of adsorption sites. | 33 |
| Figure S16. The conversion of biomass into arenes and mass balance of biomass into arenes..... | 34 |
| Figure S17. The conversion of CO ₂ into arenes and mass balance of CO ₂ into arenes | 35 |
| Author Contributions | 36 |
| Declaration of Interests | 36 |
| References | 37 |

Experimental procedures

Catalyst preparation

Nb_2O_5 was synthesized according to our previous reported procedures¹. Typically, 19.2 g of prepared niobium oxalate and 0.711 g of ammonium oxalate were dissolved in 50 mL deionized water, and then the transparent solution was aged in a Teflon-lined autoclave for 24 h at 180 °C. After cooling down, the solid was filtered, washed with distilled water and then dried at 50 °C overnight. Finally, the Nb_2O_5 sample was obtained by calcination at 400 °C for 4 h in air with a linear heating ramp of 10 °C min^{-1} . The Ru-based catalysts were prepared by the incipient wetness impregnation method with appropriate amounts of aqueous solution of RuCl_3 . The obtained samples were dried at 100 °C for 12 h and then reduced in a 10% H_2/Ar flow at 400 °C for 4 h. The metal loading in each catalyst was 2 wt%. Other supports (ZrO_2 , TiO_2 and H-ZSM-5) loaded Ru catalysts were also prepared with the incipient wetness impregnation method.

The $\text{Pd}/\text{Nb}_2\text{O}_5$ and $\text{Pt}/\text{Nb}_2\text{O}_5$ were prepared by the incipient wetness impregnation method with appropriate amounts of aqueous solution of $\text{Pd}(\text{NO}_3)_2$ and $\text{Pt}(\text{NO}_3)_2$, respectively. The obtained samples were dried at 100 °C for 12 h and then reduced in a 10% H_2/Ar flow at 300 °C for 4 h.

PET and PS were purchased from Aladdin Industrial Inc. PC was purchased from Hongyi Jiancai decoration on Taobao. PPO was purchased from Sigma Aldrich.

Catalytic test and product analysis.

The detailed reaction conditions are described in the figure captions and table footnotes. In a typical reaction with PET conversion as example, catalyst (0.1 g), PET (0.1 g) and water (10 g) were loaded into a stainless-steel autoclave reactor. After the reactor was purged with H_2

three times and charged to the target H₂ pressure (0.3 MPa), the reaction was conducted at target temperature (200 °C) with a magnetic stirring speed of 600 r.p.m. After the reaction, the reactor was quenched to ambient temperature in an ice-water bath, and the organic products were extracted using ethyl acetate when using water as solvent and analyzed by gas chromatography (GC) and GC–MS on an Agilent 7890B gas chromatograph with flame ionization detector and an Agilent 7890A GC-MS instrument, both equipped with HP-5 capillary columns (30m*250mm). The liquid solution was separated from the solid catalyst by centrifugation and was directly analyzed when octane was used as solvent. Pentadecane was used as an internal standard for the quantification of the liquid products. The product yields were calculated by using the equation: (moles of product) / (aromatic ring moles of feedstock) × 100%.

Characterization

The powder XRD patterns were recorded with a Rigaku D/max–2550VB/PC diffractometer by using Cu K α (L=0.15406 nm) radiation that was operated at 40 kV and 40 mA. The N₂ adsorption–desorption isotherms were measured at 77 K with a Micromeritics ASAP 2020 M sorption analyzer. The BET method was used to calculate the specific surface area. Transmission electron microscopy (TEM) images of samples were obtained on a JEOL Model 2100F electron microscopy at 200 kV. The actual Ru loading in the sample was detected by inductively coupled plasma–atomic emission spectroscopy (ICP-AES) on a Perkin-Elmer Optima 2100 DV spectrometer. H₂-TPR was carried out on a Micromeritics AutoChem II 2920 System in 10%H₂ /He, and 0.10 g sample was loaded. Ru K-edge XAS measurements were carried out at a public beamline, BL01B1, SPring-8, Japan. Data reduction was carried out with the Athena and Artemis ver. 0.9.26 included in the Demeter package. Quantitation of carbon

and hydrogen in plastics was done using a modified DUMAS method: samples were weighed in tin containers and combusted at high Temperature with oxygen; the resulted gases were carried by helium flow through a GC column attached to a thermal conductivity detector. Thermal gravimetric analysis (TGA) of the catalyst after first use were conducted on a Shimadzu DTG60AH simultaneous DTA-TG apparatus.

The Ru dispersion was measured by CO chemisorption using the dynamic adsorption method with an automatic chemisorbent (ChemiSorb 2720). Before adsorption, the samples (0.1 g) were reduced under pure H₂ (60 mL/min) at 473 K for 30 min (10 K/min), cooled to room temperature, and flushed in He for 30 min. Then, pulses of 5% CO in He were injected until saturation was reached, as monitored by a thermal conductivity detector (TCD). The Ru dispersion was calculated assuming a stoichiometry of 1:1 for CO adsorbed on Ru. Infrared (IR) spectra of pyridine adsorption were recorded on Nicolet NEXUS 670 FT-IR spectrometer. The samples were pressed into self-supporting disks and placed in an IR cell attached to a closed glass-circulation system. The disk was dehydrated by heating at 400 °C, for 1 h under vacuum in order to remove the physically adsorbed water. After the cell was cooled to room temperature, the IR spectrum was recorded as background. Pyridine vapor was then introduced into the cell at room-temperature until equilibrium was reached, and then a second spectrum was recorded. Subsequent evacuation was performed at 100 °C, for 10 min followed by spectral acquisitions. The spectra presented were obtained by subtracting the spectra recorded before and after pyridine adsorption.

DRIFTS of acetone adsorption were collected with a NICOLET iS50 FT-IR spectrometer equipped with an MCT/A detector. Firstly, the catalysts were pretreated *in situ* in the cell in Ar

at 400 °C for 40 min and background spectra were recorded at 200 °C, 150 °C, 100 °C, 50 °C, respectively. Then acetone with Ar was bubbled into the *in situ* cell for 40 min. Next, the cell was purged with Ar at 35 °C for 30 min and the adsorption spectra of acetone was recorded. Finally, the temperature was increased to 60 °C, 90 °C and 120 °C, respectively and the adsorption spectra of acetone were recorded at increasing temperature.

DRIFTS of toluene adsorption were collected with a NICOLET iS50 FT-IR spectrometer equipped with an MCT/A detector. Firstly, the catalysts were pretreated *in situ* in the cell in Ar at 400 °C for 40 min and background spectra were recorded at 90 °C and 35 °C respectively. Then toluene with Ar was bubbled into the *in situ* cell for 40 min. Next, the cell was purged with Ar at 35 °C for 30 min and the adsorption spectra of toluene was recorded. Finally, the temperature was increased to 90 °C and the adsorption spectra of toluene were recorded at increasing temperature.

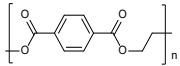
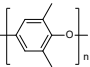
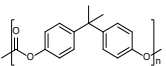
Computational details

Periodic DFT calculations for XAS simulation were performed using the CASTEP code² with the revised version of Perdew-Burke-Ernzerhof exchange-correlation functional based on the generalized gradient approximation.³ Ultrasoft pseudopotentials⁴ were constructed using the on-the-fly pseudopotential generator implemented in CASTEP to describe an excited Ru atom with a core-hole in the 1s level. The plane-wave basis set was truncated at the kinetic energy of 400 eV and a Fermi smearing of 0.1 eV was utilized. Spin-polarization was considered for all calculations. The reciprocal space was sampled using a k-point mesh with a spacing of 0.04 Å⁻¹, as generated by the Monkhorst-Pack scheme⁵. Geometry optimizations were performed on supercell structures using periodic boundary conditions. The surfaces were modeled using

metallic slabs with a thickness of eight atomic layers with 10 Å of vacuum spacing. The convergence criteria for structure optimization, energy calculation, and XANES simulation were set to the (a) self-consistent field tolerance of 1.0×10^{-6} eV per atom, (b) energy tolerance of 1.0×10^{-5} eV per atom, (c) maximum force tolerance of 0.05 eV \AA^{-1} , and (d) maximum displacement tolerance of 1.0×10^{-3} Å.

The spin-polarized density functional theory calculations were performed using Vienna Ab initio Simulation Package code (VASP)^{16,17}. Projector augmented wave (PAW) potentials were used to describe the core–valence interaction with the generalized gradient approximation (GGA), using the Perdew–Burke–Ernzerhof (PBE) functional¹⁸⁻²⁰. The DFT-D3(BJ) method was employed here in order to include van der Waals interactions²¹. For the calculations of total energy, the valence electronic states were expanded in plane wave basis sets with an energy cutoff at 450 eV and the force convergence criterion in the structure was set to 0.05 eV/\AA . The Brillouin zone was sampled using a Γ -only k-point grid in the Monkhorst–Pack scheme on HZSM-5 due to the large size. For Nb₂O₅(001) surface slab, a 15 Å thick vacuum was added along the direction perpendicular to the surface in the initial slab model to avoid the artificial interactions between the slab and its periodic images.

Table S1. Elemental analysis results of various aromatic plastics

| Substrates | Structures | Theoretical contents in pure plastic (wt %) | | Elemental analysis (wt %) | |
|-----------------------|---|---|------|---------------------------|------|
| | | C | H | C | H |
| PET |  | 62.50 | 4.17 | 62.24 | 4.28 |
| PPO |  | 80.00 | 6.67 | 78.68 | 6.21 |
| PC (polycarbonate) |  | 75.59 | 5.51 | 75.31 | 5.68 |

board)

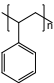
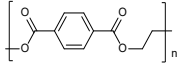
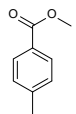
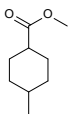
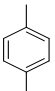
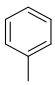
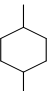
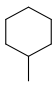
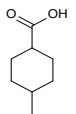
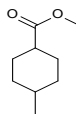
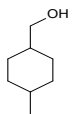
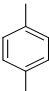
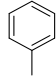
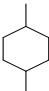
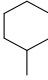
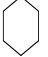
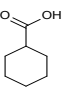
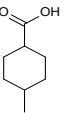
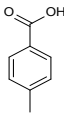
| | | | | | |
|---------------------|---|-------|------|-------|------|
| PS |  | 92.31 | 7.69 | 92.05 | 8.14 |
| Coca-Cola bottle |  | 62.50 | 4.17 | 61.94 | 4.16 |

Table S2. The conversion of methyl p-toluate and methyl 4-ethylcyclohexanecarboxylate over Ru/Nb₂O₅.

| Conversion (%) | | | | Yield (%) | | | | |
|---|---|---|---|---|---|--|---|---|
|  |  |  |  |  |  |  |  |  |
| 88.0 | - | 55.1 | 15.3 | 0.5 | 1.3 | 0.1 | 10.2 | - |
| - | 13.6 | - | - | 0.4 | 0.4 | 7.2 | - | 0.9 |
| - | > 99.9* | | | 53.6* | 36.3* | 6.5* | | 0.1* |

Reaction conditions: 0.05 g substrate, 0.025 g Ru/Nb₂O₅, 5 g H₂O, 200 °C, 3 h, 0.3 MPa H₂; * 5 g hexane, 220 °C, 4 h, 2 MPa H₂.

Table S3. The conversion of Coca-Cola bottle over Ru/Nb₂O₅.

| Yield (%) | | | | | | | | |
|---|---|---|---|---|---|--|---|-------|
|  |  |  |  |  |  |  |  | total |
| 54.2 | 17.1 | 0.5 | 9.7 | 3.2 | 4.1 | 1.5 | 0.6 | 90.9 |

Reaction conditions: 0.05 g substrate, 0.05 g Ru/Nb₂O₅, 5 g H₂O, 200 °C, 8 h, 0.3 MPa H₂.

Table S4 The catalytic conversion of PET and PS over Nb₂O₅ and without catalyst.

| Feedstock | Catalyst | Product | Yield / % |
|------------------------------|--------------------------------|-------------------|-----------|
| PET ^a | Non-catalyst | Terephthalic acid | 26.6 |
| PET ^a | Nb ₂ O ₅ | Terephthalic acid | 36.0 |
| PS ^b | Non-catalyst | - | - |
| PS ^b | Nb ₂ O ₅ | - | - |
| Diphenylmethane ^c | Non-catalyst | - | - |
| Diphenylmethane ^c | Nb ₂ O ₅ | - | - |

Reaction conditions: a, 0.1 g PET, 0.1 g catalyst, 10 g H₂O, 200 °C, 12 h, 0.5 MPa H₂; b, 0.03 g PS, 0.03 g catalyst, 4 g dodecane, 300 °C, 16 h, 0.5 MPa H₂; c, 0.1 g substrate, 0.05 g catalyst, 300 °C, 2 h, 4 g dodecane, 0.5 MPa H₂.

Table S5. Elemental analysis results of various solids.

| Solids | C (%) | H (%) | C/H |
|------------------------|-------------------|-------------------|-------|
| PS | 92.05 | 8.14 | 11.31 |
| Fresh catalyst | 0.07 | 0.95 | - |
| ^a Residue 1 | 8.98 | 1.52 | - |
| ^b Residue 2 | ^b 8.92 | ^c 0.66 | 13.52 |

^a Residue I means the catalyst-containing residual solid after reaction

^b Residue II means the residual solid after deducting C and H in fresh catalyst from Residue I

^c Calculation equation: $8.98\% - [(1 - 8.98\% - 1.52\%) \times 0.07\% / (1 - 0.07\% - 0.95\%)] \approx 8.92\%$

^d Calculation equation: $1.52\% - [(1 - 8.98\% - 1.52\%) \times 0.95\% / (1 - 0.07\% - 0.95\%)] \approx 0.66\%$

We conducted elemental analysis of various solids including fresh catalyst, the catalyst-containing residual solid after reaction (Residue I) and the residual solid after deducting C and H in fresh catalyst from Residue I (Residue II). These results show that fresh Ru/Nb₂O₅ possesses 0.95% of H, probably due to the existence of Brønsted acid sites on Nb₂O₅. After deducting C and H in fresh catalyst from the catalyst-containing residual solid after reaction, the ratio of C/H (13.52) is more than that of PS (11.31), demonstrating that PS suffered polymerization to generate denser C–C bonds networks. The polymerization products may include oligomers and carbon deposition.

Table S6. Ru contents and dispersions in various catalysts.

| Catalyst | Ru content (wt%) | Dispersion (%) |
|-----------------------------------|------------------|----------------|
| Ru/Nb ₂ O ₅ | 2.1 | 73.4 |
| Ru/ZrO ₂ | 1.9 | 21.1 |
| Ru/TiO ₂ | 2.0 | 7.7 |
| Ru/HZSM-5 | 2.0 | 15.8 |

The metal contents in the catalysts were measured by ICP-OES.

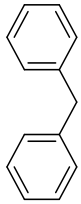
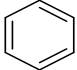
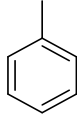
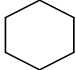
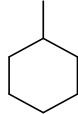
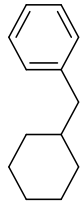
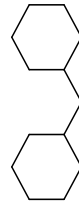
The metal dispersions were calculated based on the CO chemisorption data.

Table S7. EXAFS fitting results of the Ru K-edge for Ru/TiO₂ and Ru/ZSM-5.

| Sample | S_0^2 | shell | CN | R (Å) | ΔE_0 (eV) | σ^2 (Å ²) | R -factor (R^2) |
|---------------------|-------------|-------|------------|-------------|-------------------|------------------------------|-----------------------|
| Ru foil | 0.902 | Ru–Ru | 12.0 (fix) | 2.68 ± 0.00 | 1.8 ± 0.7 | 0.004 ± 0.000 | 0.005 |
| Ru/TiO ₂ | 0.902 (fix) | Ru–Ru | 9.0 ± 1.4 | 2.67 ± 0.01 | −0.9 ± 1.6 | 0.007 ± 0.001 | 0.008 |
| Ru/HZSM-5 | 0.902 (fix) | Ru–Ru | 9.1 ± 1.2 | 2.67 ± 0.01 | 1.9 ± 1.4 | 0.006 ± 0.001 | 0.006 |

$E_0 = 25125$ eV, k -weigh: 3, k -range: 3.0~16, R -range: 2.1~2.9

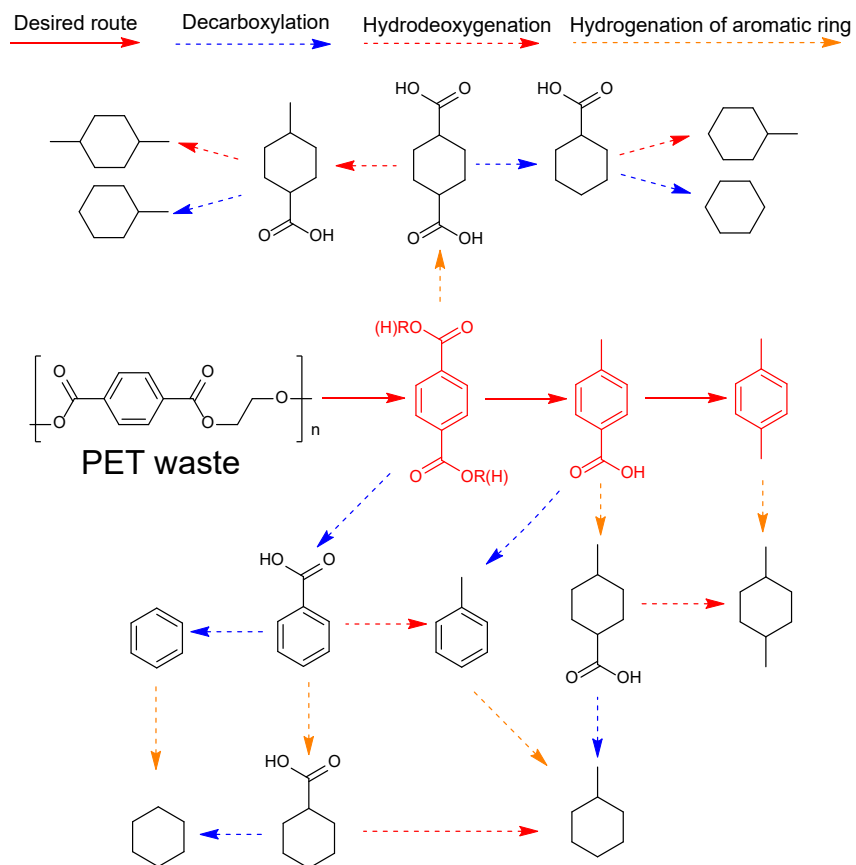
Table S8. The conversion of diphenylmethane over Ru/Nb₂O₅ and Ru/HZSM-5

| Catalyst | Conversion (%) | Yield (%) | | | | | | Total (%) |
|-----------------------------------|---|---|---|---|---|---|---|-----------|
| |  |  |  |  |  |  |  | |
| Ru/Nb ₂ O ₅ | 54.3 | 23.9 | 13.1 | - | - | 8.2 | 0.9 | 46.1 |
| Ru/HZSM-5 | 17.6 | - | - | 1.4 | 0.8 | 2.0 | 0.3 | 4.5 |

Reaction conditions: 0.1 g diphenylmethane, 0.05 g dodecane, 5 g H₂O, 300 °C, 3 h, 0.3 MPa H₂.

Table S9. The amount of Brønsted and Lewis acid sites on Nb₂O₅ and HZSM-5

| Sample | Acid from Py-FTIR / $\mu\text{mol g}^{-1}$ | | |
|--------------------------------|--|-------|-------|
| | Brønsted | Lewis | Total |
| Nb ₂ O ₅ | 99.1 | 276.5 | 375.6 |
| HZMS-5 | 447.8 | 175.2 | 623.0 |



Scheme S1. Proposed reaction pathway for the conversion of PET.

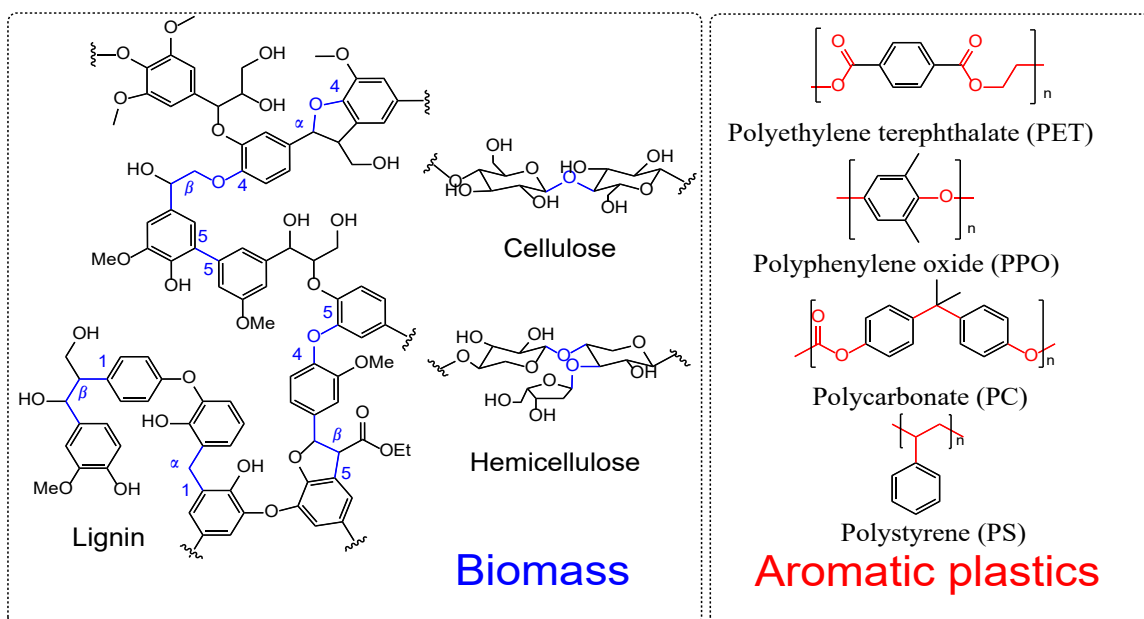


Figure S1. View of representative C-O and C-C linkages of biomass and aromatic plastics.

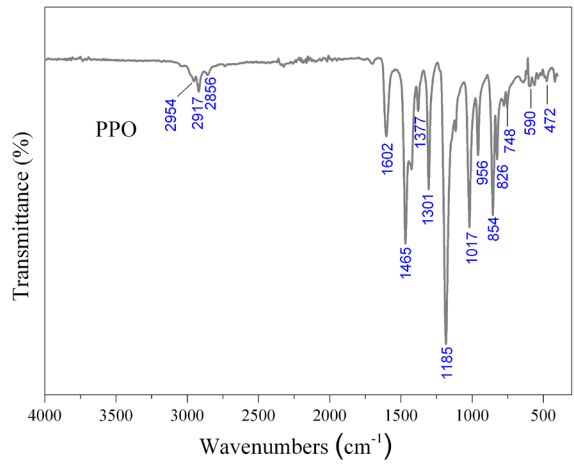
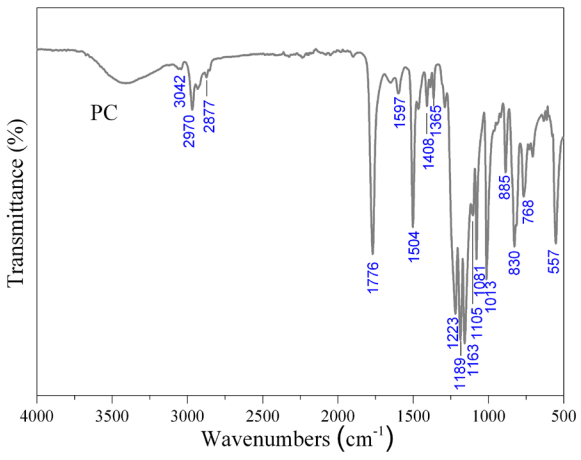
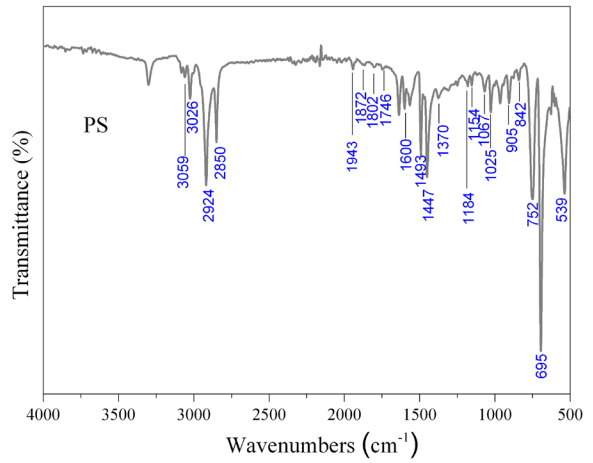
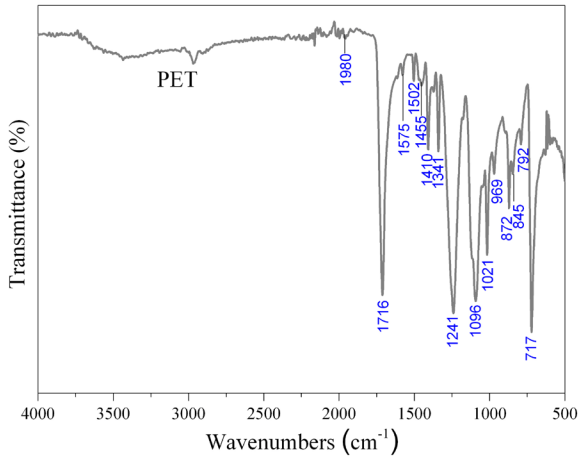


Figure S2. IR results of various plastics

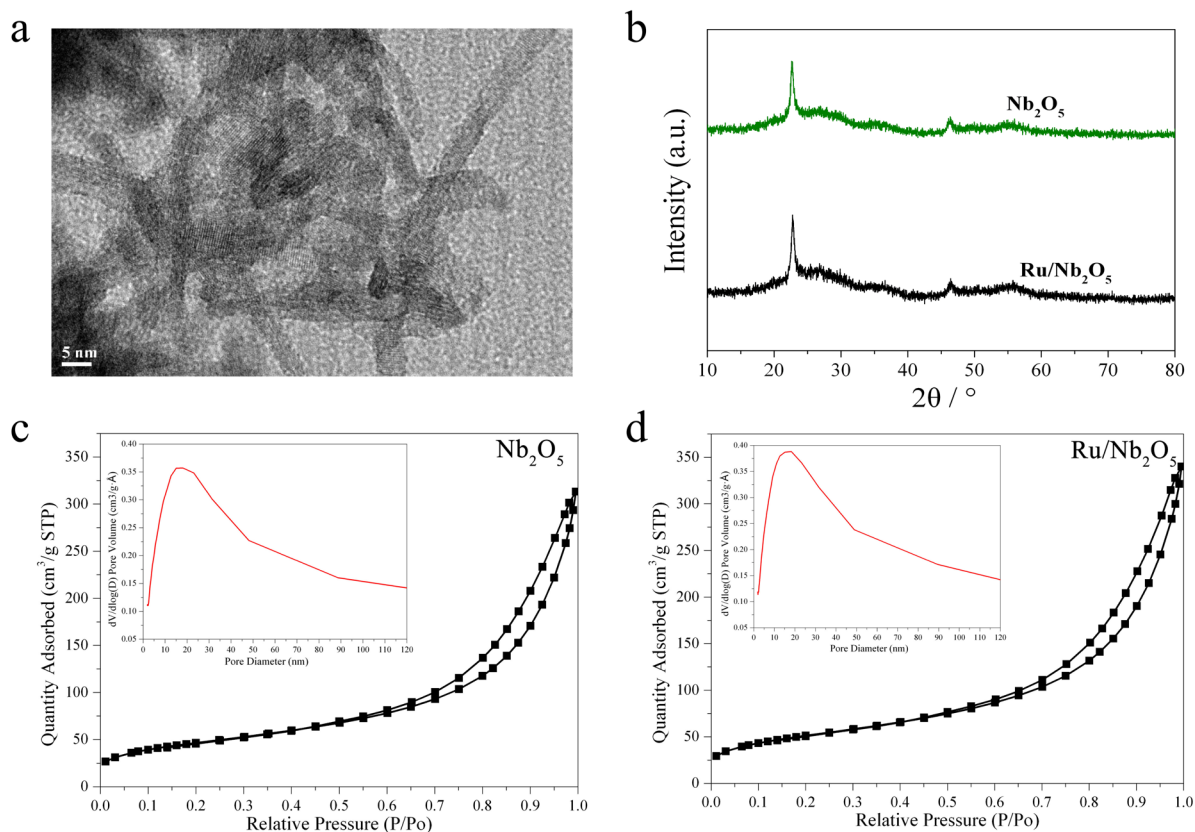


Figure S3. (a) TEM images of Ru/Nb₂O₅, (b) XRD patterns of Nb₂O₅ and Ru/Nb₂O₅, (c) N₂ adsorption-desorption isotherms and the BJH pore size distribution curves of Nb₂O₅, (d) N₂ adsorption-desorption isotherms and the BJH pore size distribution curves of Ru/Nb₂O₅.

TEM images, XRD patterns, N₂ adsorption-desorption isotherms and the BJH pore size distribution curves of catalysts are provided in Figure S3. The TEM images of Ru/Nb₂O₅ show that no Ru species were found. This is consistent with the finding by other techniques that the Ru species on Nb₂O₅ to be small and highly dispersed. Although Nb₂O₅ shows a well-defined nanorod shape, its microscopic atom arrangement presents a layered structure^[23,24]. Two diffraction peaks at 22.7° and 46.2° were observed, further revealing its layered structure and low degree of crystallinity. N₂ adsorption-desorption isotherms and the BJH pore size distribution curves of Nb₂O₅ show that its pore structure is formed through nanosheet stacking. After loading Ru species, the porous properties of the Nb₂O₅ have no obvious change and the average pore size of Nb₂O₅ and Ru/Nb₂O₅ are 9.42 nm and 9.41 nm, respectively. These results

confirm that the loading of Ru species does not affect the porous properties of the Nb₂O₅ support.

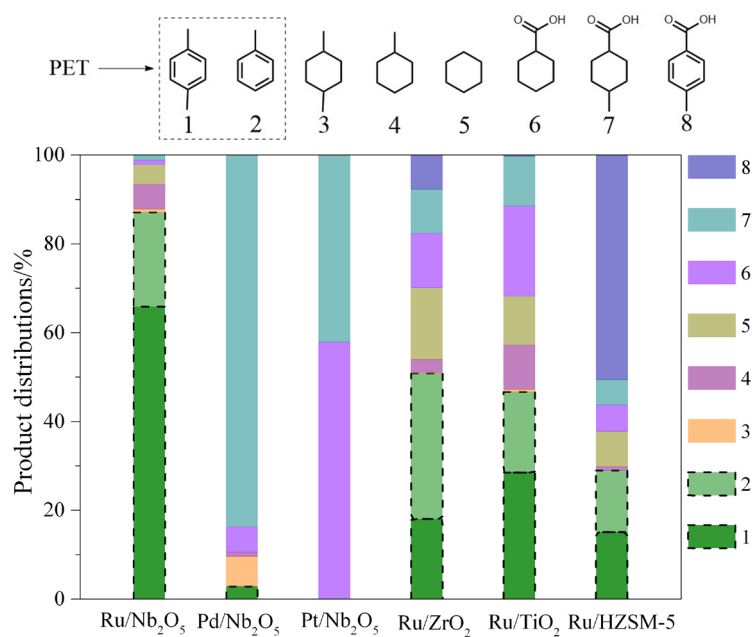


Figure S4. The direct conversion of PET over various catalysts. Reaction conditions: 0.1 g PET, 0.1 g catalyst, 10 g H₂O, 200 °C, 12 h, 0.3 MPa H₂

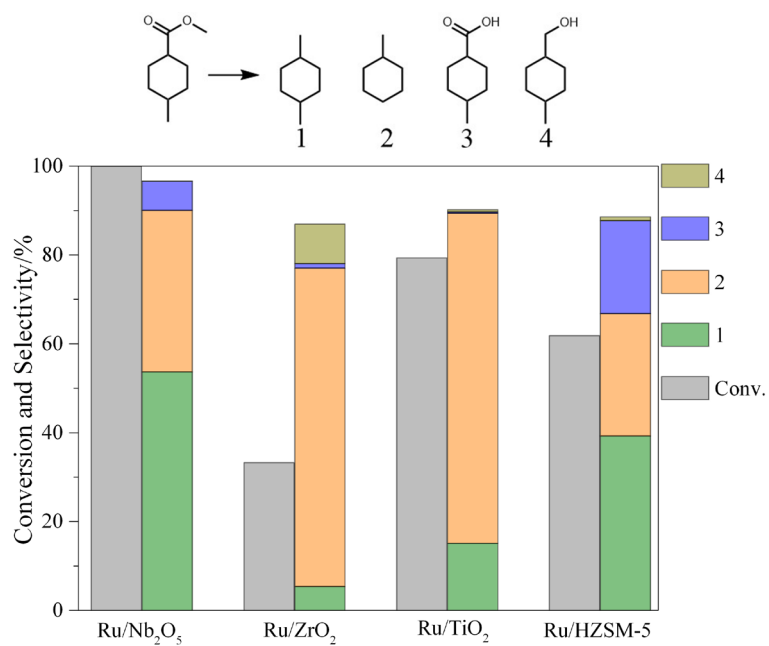


Figure S5. The conversion of methyl 4-methylcyclohexanecarboxylate over various catalysts. Reaction conditions: 0.05 g methyl 4-methylcyclohexanecarboxylate, 0.025 g catalyst, 5 g hexane, 220 °C, 4 h, 3 MPa H₂.

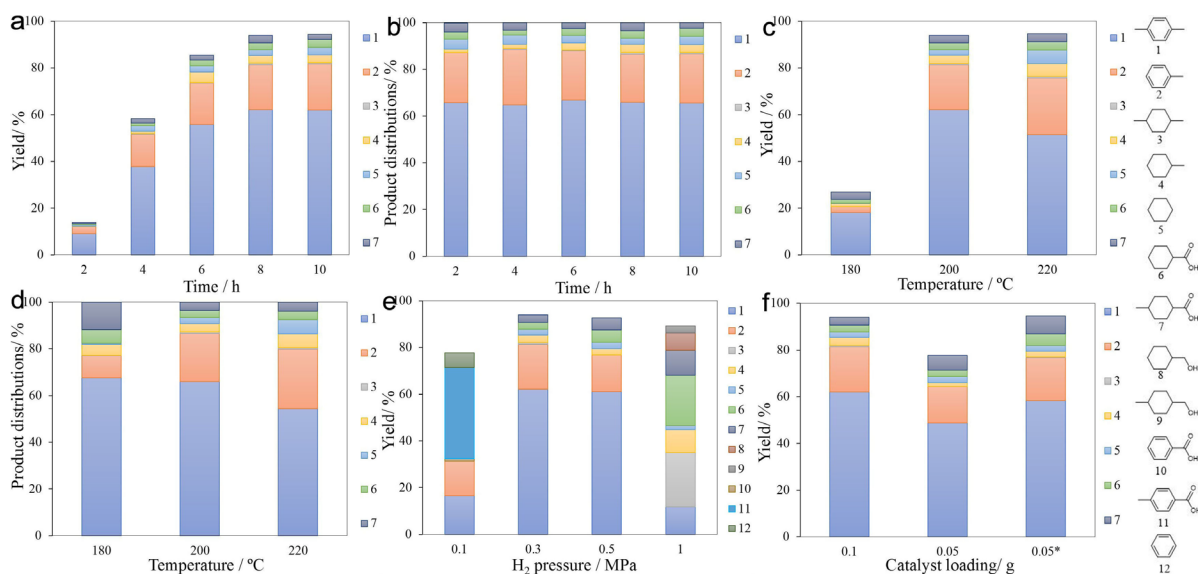


Figure S6. Influence of reaction conditions in the conversion of PET over Ru/Nb₂O₅. (a) yield versus reaction time, (b) product distributions versus reaction time, (c) yield versus reaction temperature, (d) product distributions versus reaction temperature, (e) yield versus H₂ pressure, (f) yield versus catalyst loading. Reaction conditions: (a, b) 0.1 g PET, 0.1 g Ru/Nb₂O₅, 10 g H₂O, 200 °C, 0.3 MPa H₂. (c, d) 0.1 g PET, 0.1 g Ru/Nb₂O₅, 10 g H₂O, 8 h, 0.3 MPa H₂. (e) 0.1 g PET, 0.1 g Ru/Nb₂O₅, 10 g H₂O, 200 °C, 8 h. (f) 0.1 g PET, 10 g H₂O, 200 °C, 8 h, 0.3 MPa H₂. *0.1 g PET, 10 g H₂O, 200 °C, 16 h, 0.3 MPa H₂.

In an attempt to explore the influence of reaction conditions, we have optimized the reaction conditions including time, temperature, hydrogen pressure and catalyst loading.

Yield and product distribution versus reaction time (Figure S6a and S6b) show that the yield of total products increased with prolonging the reaction time from 2 to 10 h, but the product distribution has not obvious change, indicating the reaction follows a parallel pathway and with the direct hydrodeoxygenation as the main pathway over Ru/Nb₂O₅.

Yield and product distribution versus reaction temperature (Figure S6c and S6d) show that the yield (from 18.1 to 62.1%) of *p*-xylene tends to increase with the increase of temperature from 180 °C to 200 °C. While further increasing the temperature to 220 °C, the yield of *p*-xylene decreased to 51.5% with an increase of decarboxylation products (toluene

and cyclohexane) (from 21.7 to 30.0%). This result indicates that lower temperature leads to a slow reaction rate, whereas higher temperature favors the undesirable decarboxylation.

Yield versus H₂ pressure (Figure S6e) shows that a large amount of ring-saturated products were formed at 1 MPa, whereas more oxygenated compounds were achieved at 0.1 MPa. This result demonstrates that higher pressure favors the hydrogenation of aromatic ring, whereas lower pressure is not able to completely deoxidize. A suitable pressure range of 0.3-0.5 MPa affords the desirable outcome.

Yield versus catalyst loading (Figure S6f) shows that when the ratio of catalyst loading/substrate was reduced from 1/1 to 1/2, the total monomer yield was reduced from 94.0 to 77.9% and the product distribution remained nearly unchanged. The total monomer yield can be increased to 94.6% via prolonging reaction time, meanwhile no obvious change in the selectivity of arenes.

We conducted the solvent-free conversion of PET under the same conditions and found that no depolymerization products in both liquid and gas phases were detected, indicating that solvent-free depolymerization of PET to monomers or other gas molecules cannot occur under the this reaction conditions, likely due to restricted mass transfer. Consequently, water seems to be necessary to perform the reaction.

We tested the gas composition after reaction and indeed observed the formation of a small amount of methane and ethane. Methane may be generated via CO₂ (come from partially decarboxylation) hydrogenation and ethane is from the ethyl framework of PET. The pH values of the water before (6.20) and after (6.25) reaction have no obvious change.

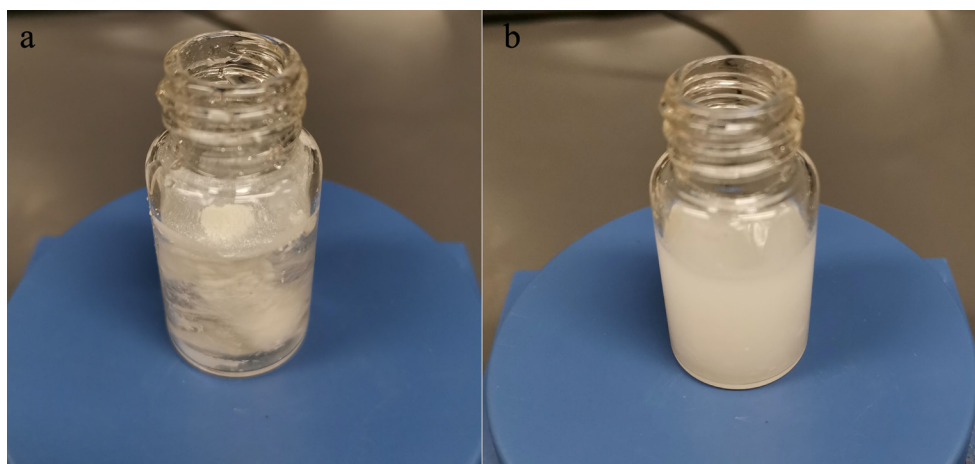


Figure S7. The observations for dispersity of PPO in water and octane through stirring at room temperature. (a) in water; (b) in octane.

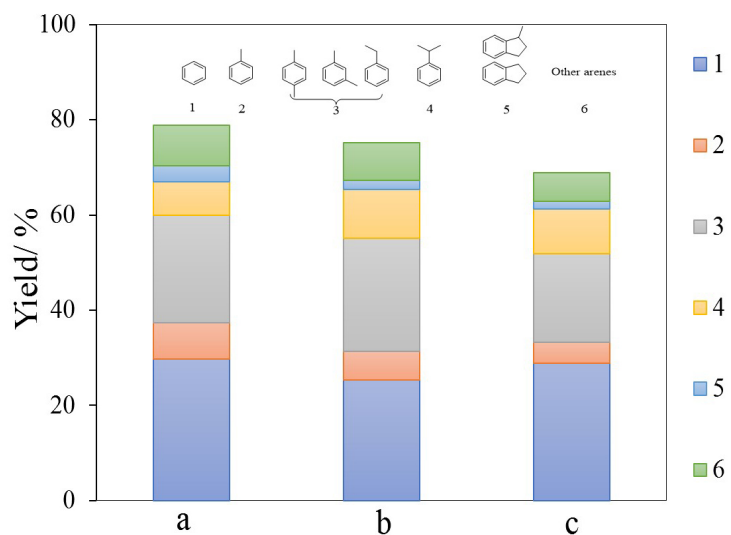


Figure S8. The conversion of mixed plastics with different concentration of substrate and different substrate/catalyst mass ratio. Reaction conditions: 15 mg PET, 15 mg PC, 15 mg PS, 15 mg PPO, 320 °C, 16 h, 0.5 MPa H₂. (a) 60 mg Ru/Nb₂O₅, 4 g octane, (b) 60 mg Ru/Nb₂O₅, 2 g octane; (c) 30 mg Ru/Nb₂O₅, 4 g octane.

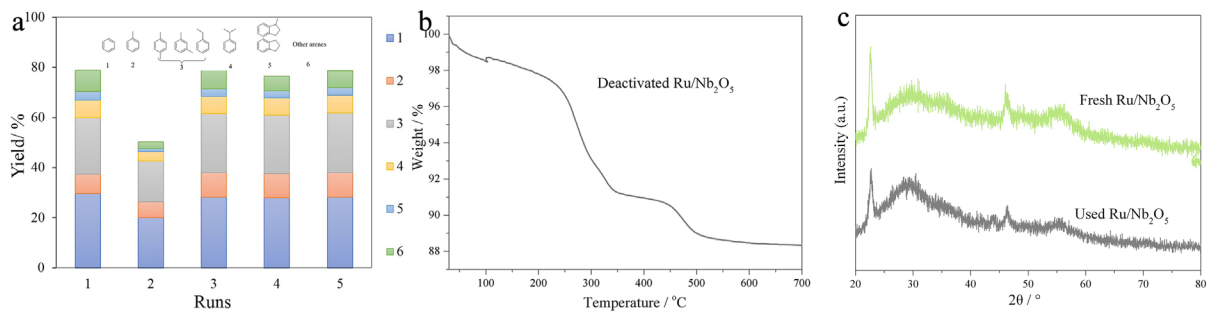


Figure S9. Recyclability test of Ru/Nb₂O₅ for the conversion of mixed plastics. (a) reaction conditions: 15 mg PET, 15 mg PC, 15 mg PS, 15 mg PPO, 60 mg Ru/Nb₂O₅, 4 g octane, 320 °C, 16 h, 0.5 MPa H₂; (b) TG profile of deactivated Ru/Nb₂O₅ catalyst after first run; (c) XRD patterns of fresh Ru/Nb₂O₅ and used Ru/Nb₂O₅ after five runs.

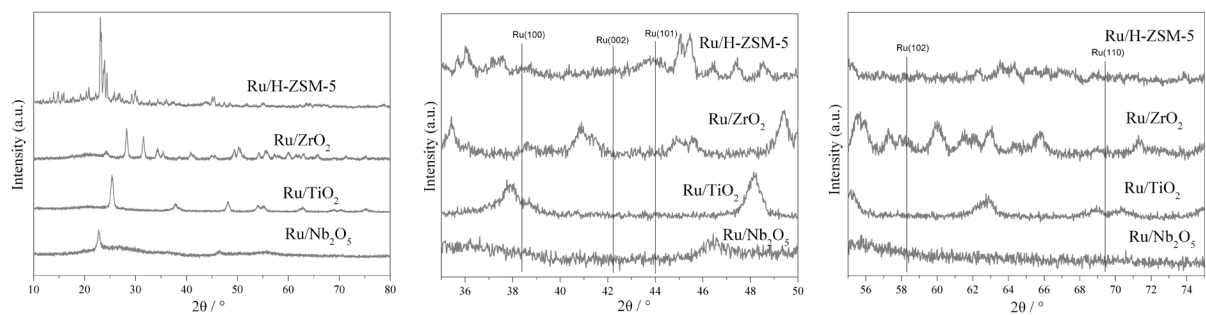


Figure S10. XRD patterns of various catalysts and their larger versions (35-50° and 55-75°).

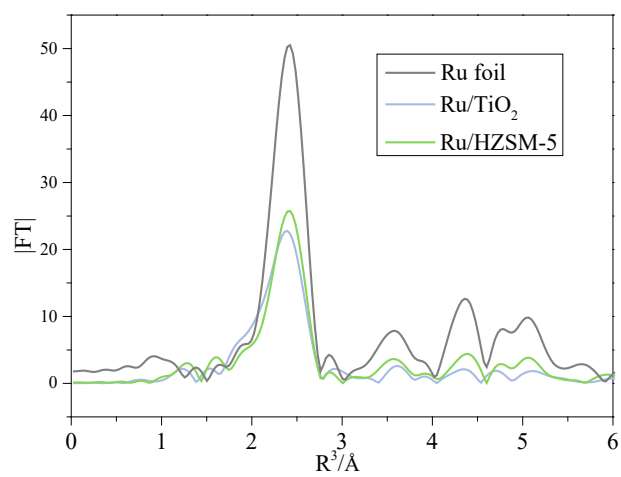


Figure S11. EXAFS spectra of Ru/TiO₂ and Ru/ZSM-5.

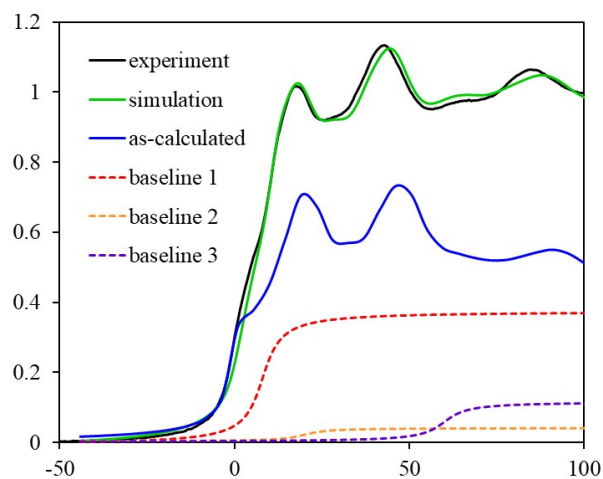


Figure S12. XANES simulation for Ru foil based on DFT calculation. The simulation represents sum of as-calculated spectrum of bulk Ru and baselines 1–3. Three arctangent functions were generated as baselines for calibration so that the simulation well reproduce the experimental spectrum. These baselines were also used for XANES simulation of other Ru surfaces.

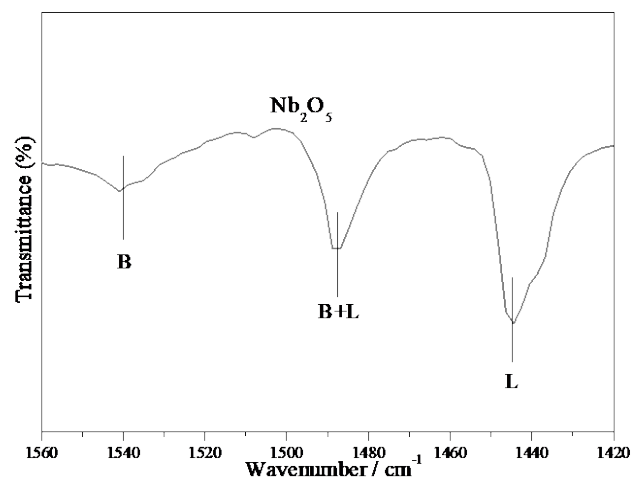


Figure S13. Py-FTIR spectra collected after treatment at 100 °C under vacuum of Nb₂O₅.

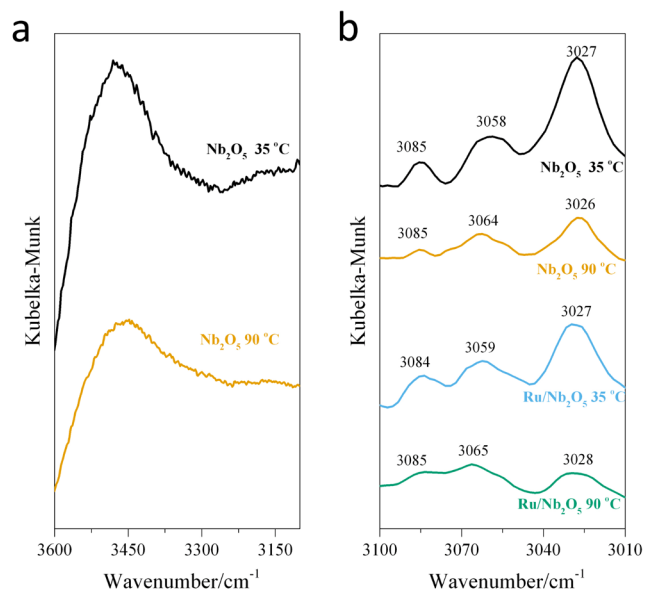


Figure S14 Toluene DRIFTS spectra of Ru/Nb₂O₅ and Nb₂O₅

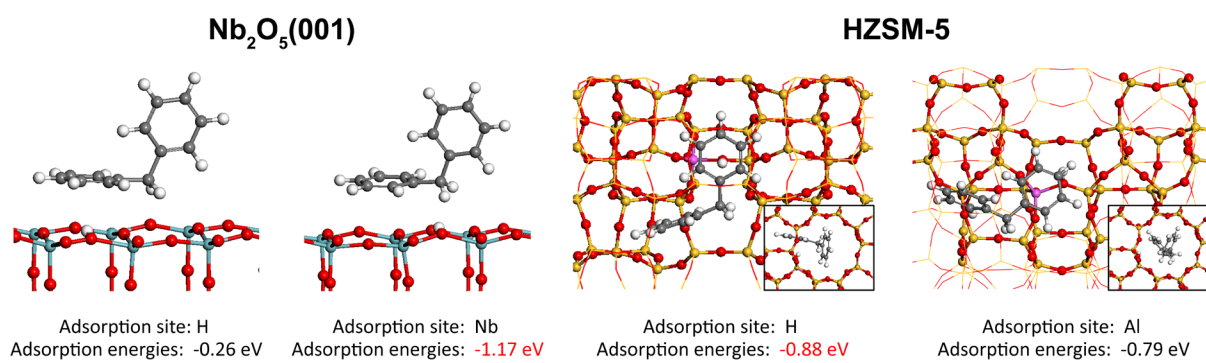


Figure S15 The optimization of adsorption sites.

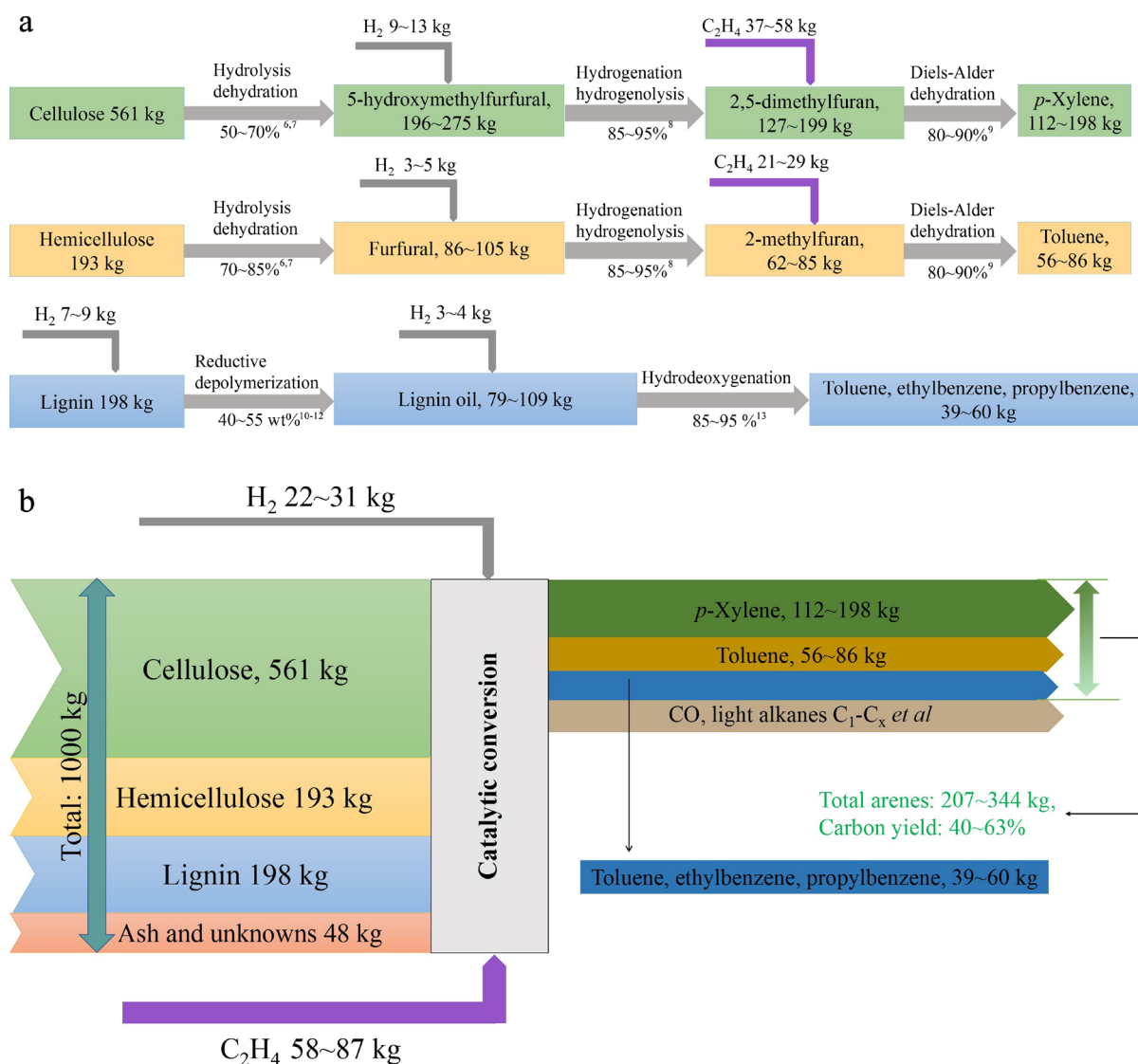


Figure S16. (a) The conversion of biomass into arenes; (b) Mass balance of biomass (birch¹⁴) into arenes (assuming the conversion of 1 ton feedstocks).

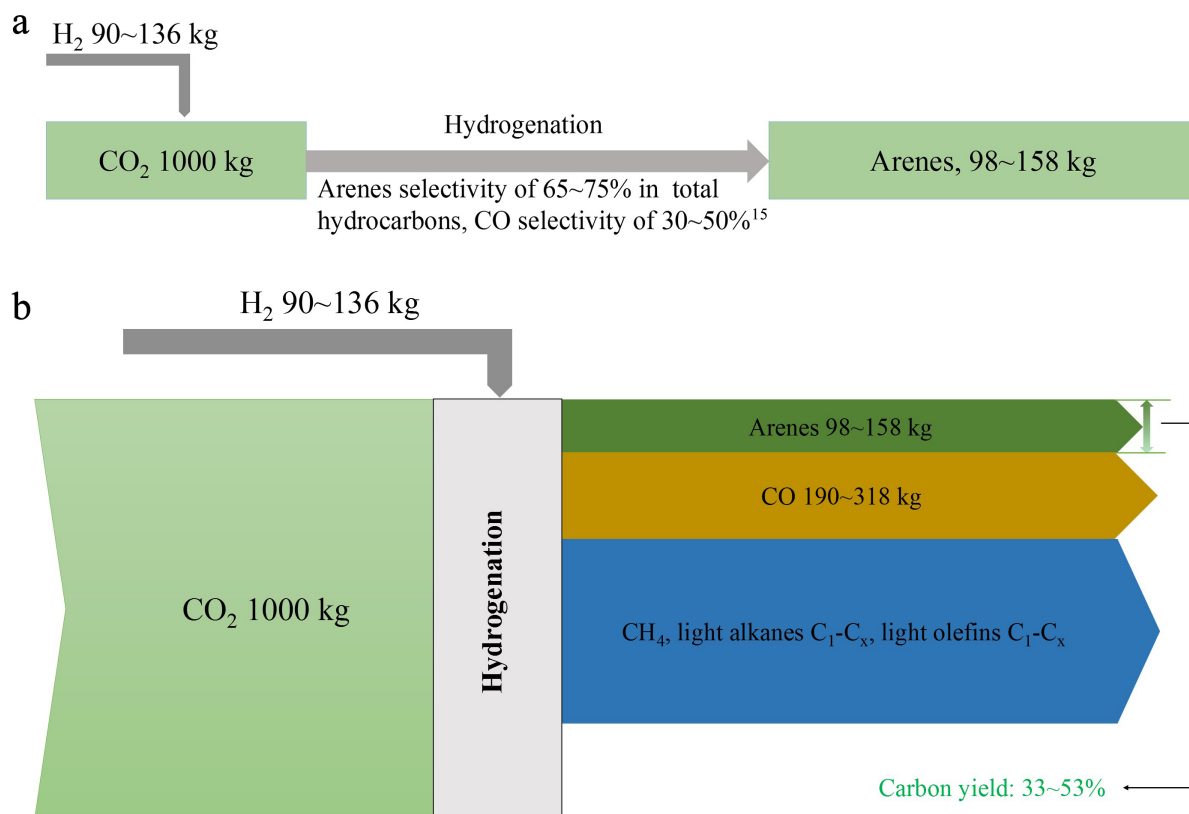


Figure S17. (a) The conversion of CO_2 into arenes; (b) Mass balance of CO_2 into arenes (assuming the conversion of 1 ton CO_2).

Author Contributions

Y.W. and N.Y. conceived and supervised the project. Y.W., N.Y. and Y.J. designed experiments. Y.J. C.S. X.L. and Y.G. performed the synthesis, characterisation, catalytic testing and process analysis. S.F. conducted XAS measurement, analysis and DFT simulation of XANES spectra. J.X. and H.W. conducted DFT calculations of C-C cleavage process. M.H. participated in DFT calculations. Y.J. Y.W. and N.Y. wrote the manuscript. All authors participated in discussions and paper preparation.

Declaration of Interests

The authors declare no competing interests.

References

1. Jing, Y. X., Xin, Y., Guo, Y., Liu, X. H., and Wang, Y. *Chin. J. Catal.* **2019**, *40*, 1168-1177.
2. Segall, M. D., Lindan, P. J. D., Probert, M. J., Pickard, C. J., Hasnip, P. J., Clark, S. J., and Payne, M. C. *Condens. Mat.* **2012**, *14*, 2717-2744.
3. Hammer, B., Hansen, L. B., and Nørskov, J. K. *Phys. Rev. B* **1999**, *59*, 7413-7421.
4. Vanderbilt, D. *Phys. Rev. B* **1990**, *41*, 7892-7895.
5. Monkhorst, H. J., and Pack, J. D. *Phys. Rev. B* **1967**, *13*, 5188-5192.
6. Wang, H.; Zhu, C.; Li, D.; Liu, Q.; Tan, J.; Wang, C.; Cai, C.; Ma, L., *Renew. Sustain. Energy Rev.* **2019**, *103*, 227-247.
7. Esteban, J.; Vorholt, A. J.; Leitner, W., *Green Chem.* **2020**, *22*, 2097-2128
8. Shuo, C.; Robert, W.; Franck, D.; Eric, M.; Sébastien, R., *Chem. Rev.* **2018**, *118*, 11023–11117
9. Settle, A. E.; Berstis, L.; Rorrer, N. A.; Roman-Leshkóv, Y.; Beckham, G. T.; Richards, R. M.; Vardon, D. R., *Green Chem.* **2017**, *19*, 3468-3492.
10. Huang, X.; Gonzalez, O. M. M.; Zhu, J.; Korányi, T. I.; Boot, M. D.; Hensen, E. J., *Green Chem.* **2017**, *19*, 175-187.
11. Schutyser, W.; Renders, T.; Van den Bosch, S.; Koelewijn, S. F.; Beckham, G. T.; Sels, B. F., *Chem. Soc. Rev.* **2018**, *47*, 852-908.
12. Sun, Z. H.; Fridrich, B.; de Santi, A.; Elangovan, S.; Barta, K., *Chem. Rev.* **2018**, *118*, 614-678.
13. Jing, Y.; Dong, L.; Guo, Y.; Liu, X.; Wang, Y., *ChemSusChem* **2019**, doi:10.1002/cssc.201903174.
14. Li, C.; Zheng, M.; Wang, A.; Zhang, T., *Energy Environ. Sci.* **2012**, *5*, 6383-6390.
15. Zhou, W.; Cheng, K.; Kang, J.; Zhou, C.; Subramanian, V.; Zhang, Q.; Wang, Y., *Chem. Soc. Rev.* **2019**, *48*, 3193-3228.
16. Kresse, G.; Furthmüller, J. *Comput. Mater. Sci.* **1996**, *6*, 15-50.
17. Kresse, G.; Furthmüller, J. *Phys. Rev. B: Condens. Matter Mater. Phys.* **1996**, *54*, 11169-11186.
18. Perdew, J. P.; Burke, K.; Ernzerhof, M. *Phys. Rev. Lett.* **1996**, *77*, 3865-3868.
19. Kresse, G.; Joubert, D. *Phys. Rev. B: Condens. Matter Mater. Phys.* **1999**, *59*, 1758-1775.
20. Blöchl, P. E.; Jepsen, O.; Andersen, O. K. *Phys. Rev. B: Condens. Matter Mater. Phys.* **1994**, *49*, 16223-16233.
21. Grimme, S.; Ehrlich, S.; Goerigk, L. *J. Comp. Chem.* **2011**, *32*, 1456-1465.
22. T. Murayama, J. Chen, J. Hirata, K. Matsumoto, W. Ueda, *Catal. Sci. Technol.* **2015**, *4*, 4250–4257.
23. Y. Xin, L. Dong, Y. Guo, X. Liu, Y. Hu, Y. Wang, *J. Catal.* **2019**, *375*, 202–212.